Chapter 2
Physics of Propagation-Based X-Ray Tomography

On 8 November 1895 Wilhem Conrad Röntgen discovered X-rays and, few weeks later, the famous radiograph of Mrs Röntgen's hand was imaged, marking the beginning of a new scientific discipline: radiography [1, 2]. After more than a century of unprecedented scientific, technical and technological development, clinical radiological exams, with only few exceptions, still rely on the same contrast formation mechanism, which is X-ray attenuation. Despite the immense success of conventional attenuation-based (also referred to as absorption-based) radiography and its widespread use as diagnostic tool, the advent of synchrotron radiation (SR) facilities producing intense and coherent X-ray beams allowed the researchers to focus their attention on an alternative image contrast mechanism, the phase contrast.

Phase contrast relies on the phase shift experienced by X-rays when traversing matter rather than their attenuation. In fact, the interpretation of X-rays as electromagnetic waves with a wavelength much shorter ($\sim$10,000 times) than visible light was already known at the beginning of XX century and, as stated in the far-sighted Nobel Lecture given by A. H. Compton in 1927: "[…] there is hardly a phenomenon in the realm of light whose parallel is not found in the realm of X-rays […]" [3]. This means that X-ray imaging can also take advantage of those interactions affecting the phase of the incoming wave (e.g.., refraction), which are well understood and described for visible and nearly-visible light wavelengths. The experimental arrangements allowing the detection of these effects are the so-called phase-sensitive techniques, while an image exhibiting a contrast due to phase effects is referred to as phase-contrast image.

The advent of digital detectors and powerful computers in 1970s promoted another major breakthrough in the field of diagnostic radiology, whose magnitude is comparable with the discovery of X-rays itself: computed tomography (CT) allowed for the first time to investigate bulk samples by reconstructing maps, i.e. 'slices', of their properties along the X-rays propagation plane [4]. To obtain a tomographic image, or tomogram, one needs to acquire a certain number of radiographic images,
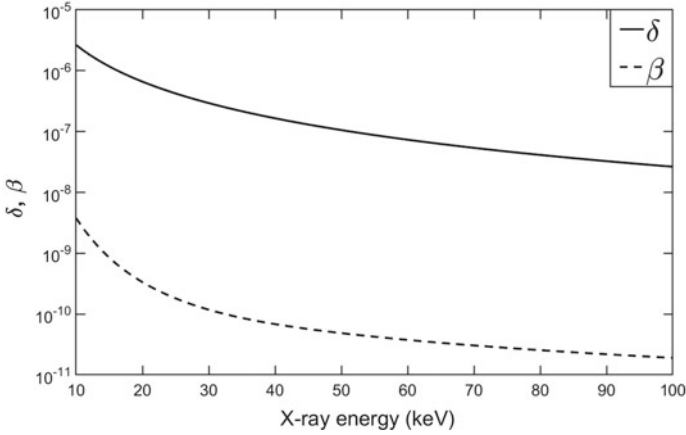
Fig. 2.1 Values of δ and β for polymethyl methacrylate (PMMA), often used as a tissue equivalent material in phantoms, between 10 and 100 keV. The semi-logarithmic plot highlights their 2–3 orders of magnitude difference spanning a broad energy range. Data from publicly available database [5]

or projections, at different angular positions of the sample. The projections are then fed into a reconstruction algorithm which inverts the tomographic problem yielding a virtually reconstructed map (or stack of maps) of the object's properties. CT was first developed in the context of conventional radiography to create X-ray attenuation maps but, given the rather general formulation of the tomographic problem, it can be in most cases straightforwardly extended to phase-contrast images, yielding, for instance, phase or even scattering maps.

This chapter is entirely devoted to explaining the physics underlying phase-contrast formation mechanism, detailing the advantages over conventional attenuation-based radiography/tomography of one of the most widespread phase-sensitive techniques, propagation-based imaging. Starting from rather general concepts, a mathematical model describing X-ray refraction will be introduced in the next section; this general model, which constitutes a common ground for many phase-sensitive techniques, will be further specialized to describe the propagation-based image formation process, also considering non perfectly coherent sources, and its inverse problem, namely the phase retrieval. Finally, the discussion will be extended to the tomographic reconstruction in the specific context of propagation-based imaging.

2.1   X-Rays Through Matter: Attenuation and Refraction

Let us consider a parallel and monochromatic beam travelling in vacuum along the z axis. In the wave formalism this can be described as a plane wave, whose space-dependent component can be written as

$$\psi = \psi_0 \, e^{ikz} \tag{2.1}$$

where ψ_0 is its real-valued amplitude, $k = |\mathbf{k}| = 2\pi/\lambda$ is the wave number and $\mathbf{k}$ is the wave vector pointing in the propagation direction, while λ is the wavelength. When the wave propagates through a medium, the wave number must be replaced by $k_{medium} = nk$, n being the complex-valued refractive index. For X-rays n is usually written as $n = 1 - \delta + i\beta$, where δ and β are real, positive and very small numbers, related, as it will be clear in the following, to the phase-shift and absorption/attenuation properties of the medium, respectively [6]. Of note, the real component of the refractive index is smaller than one, meaning that the phase-velocity in a medium is higher than the speed of light; of course this does not violate relativity as the group velocity still does not exceed the speed of light in vacuum [7]. For X-rays with energies sufficiently higher than the absorption edges of the medium, that for light materials (e.g., soft tissues) are below few keV, δ can be calculated in classical electrodynamics as

$$\delta \simeq r_0 \rho_e \lambda^2 / 2\pi \tag{2.2}$$

$r_0 = 2.82 \times 10^{-15}$ m being the classical electron radius and ρ_e the electron volume density; conversely, β is found to be proportional to λ^3 [8]. Despite being both small numbers, for biological samples and energies of interest in soft-tissue biomedical imaging (i.e. tens of keV), δ is approximately 3 orders of magnitude larger than β, their typical values being $10^{-6} - 10^{-7}$ and $10^{-9} - 10^{-10}$, respectively, as shown in Fig 2.1 [9, 10]. This huge difference is the reason why phase-sensitive techniques can be advantageous over attenuation-based imaging.

To understand how the presence of a sample can affect both amplitude and phase of the incoming X-ray wave, let us consider an object described by a three-dimensional distribution of refractive index $n(x, y, z) = 1 - \delta(x, y, z) + i\beta(x, y, z)$, traversed by the wave defined in Eq. (2.1), as schematically depicted in Fig 2.2. After the interaction with the object, the X-ray wave $\psi_{out}(x, y)$ at a given position in the object plane (x, y) will be the incident wave modulated by a complex transmission factor $T(x, y)$ [11]:

$$\psi_{out}(x, y) = \psi T(x, y) = \psi_0 e^{ikz} T(x, y) \tag{2.3}$$

where $T(x, y)$ is function of the object refractive index distribution and it is written as

$$T(x, y) = e^{ik \int (n(x,y,z)-1) \, dz} = e^{-k \int \beta(x,y,z) \, dz} \, e^{-ik \int \delta(x,y,z) \, dz} \tag{2.4}$$

with the line integral extending over the object thickness along z direction. The transmission function can be computed directly from Maxwell's equations assuming the object to be non-magnetic, with null charge and current densities [12]. Moreover, the above description implicitly assumes the so-called projection approximation to hold, meaning that the changes in the local direction of the wave vector within the sample
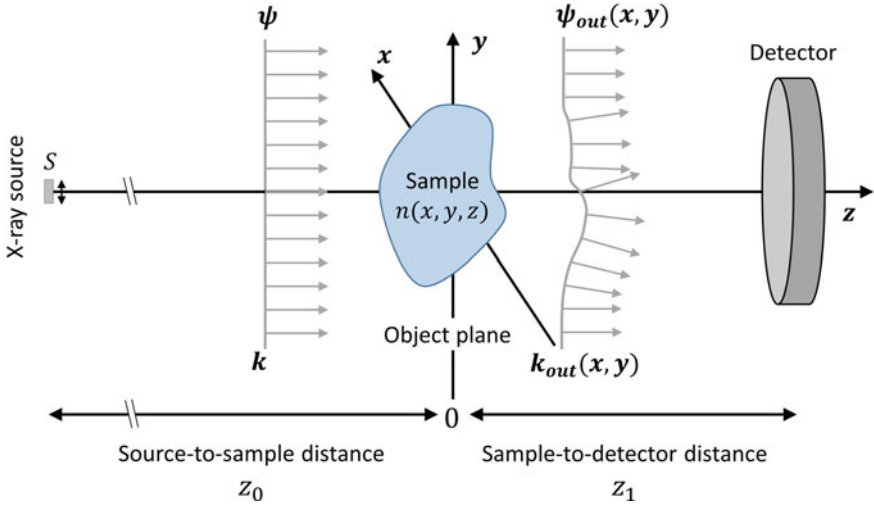
Fig. 2.2 Sketch of wave-object interaction. ψ is a monochromatic plane wave with wave vector **k** impinging on the sample described by its refractive index distribution $n(x, y, z)$. The wavefront emerging from the sample $\psi_{out}(x, y)$ is modulated both in amplitude and phase by the object and has a local wave vector $\mathbf{k_{out}}(x, y)$. z_0 and z_1 are, respectively, the source-to-sample and the sample-to-detector distances while s is the source size

are considered to be negligible. In a more pictorial description, the refraction effects are considered to be 'accumulated' through the object and to manifest themselves at its exit surface. In this way the net effect of the refractive object on the wave field can be expressed as an integral along the propagation direction of the impinging wave [13]. The previous equation implies that the object modulates the X-ray wave by reducing its amplitude by a factor dependent on β, and it introduces a shift in its phase dependent on δ, that can be written as $\Phi(x, y) = -k \int \delta(x, y, z) \, dz$.

Considering conventional radiographic techniques which are only sensitive to the transmitted X-ray intensity, i.e. the square modulus of the wave, Eq. (2.3) reduces to

$$|\psi_{out}(x, y)|^2 = |\psi_0 e^{ikz} T(x, y)|^2 = \psi_0^2 e^{-2k \int \beta(x, y, z) \, dz} \tag{2.5}$$

The latter equation can be immediately identified with the well-known Beer-Lambert law [14], describing the X-ray attenuation through an object:

$$I(x, y) = I_0 e^{-\int \mu(x, y, z) \, dz} \tag{2.6}$$

where I_0 is the beam intensity impinging on the object and $\mu = 2k\beta$ is its attenuation coefficient. At this point it is clear that in conventional imaging the phase-shift term introduced in Eq. (2.4) does not play any role at all. Conversely, the goal of any phase-sensitive technique is to detect the change in phase which, since $\delta \gg \beta$, is much bigger than attenuation.

Going back to the wave model, the phase-shift term Φ is interpreted as a local distortion of the wavefront that, at a given point of the object plane, will have a slightly different propagation direction with respect to the impinging planar wave. To determine the outgoing propagation direction at each point we assume the deviations from the initial direction z to be small (i.e. paraxial approximation) or, more formally, that the absolute values of the spatial derivatives $|(\partial/\partial x)\,\Phi(x, y)|$ and $|(\partial/\partial y)\,\Phi(x, y)|$ are much smaller than the wave number k. In this way the outgoing wave vector reads

$$\mathbf{k_{out}}(x,\, y) = \left(\frac{\partial}{\partial x}\Phi(x,\, y)\right)\hat{\mathbf{x}} + \left(\frac{\partial}{\partial y}\Phi(x,\, y)\right)\hat{\mathbf{y}} + k\hat{\mathbf{z}} \qquad (2.7)$$

where $\hat{\mathbf{x}}$, $\hat{\mathbf{y}}$ and $\hat{\mathbf{z}}$ are unit vectors pointing along x, y and z directions, respectively. The deviation with respect to the original direction $\hat{\mathbf{z}}$ imparted to the beam by the refractive object is expressed as a position-dependent refraction angle $\alpha(x,\, y)$ which is written as

$$\alpha(x,\, y) \simeq \frac{1}{k}\sqrt{\left(\frac{\partial}{\partial x}\Phi(x,\, y)\right)^2 + \left(\frac{\partial}{\partial x}\Phi(x,\, y)\right)^2} = \frac{1}{k}|\nabla_{xy}\Phi(x,\, y)| \qquad (2.8)$$

where ∇_{xy} is the gradient operator in the object plane.

Equation (2.8) is a central result of this section and provides the link between a detectable physical quantity, the refraction angle, and the object-induced phase shift. In this context, the goal of many phase-sensitive techniques will be somehow to convert this refraction angle into intensity modulations on the detector. Before describing how this can be achieved experimentally, it is worth noting that for biomedical applications (i.e. $\delta \sim 10^{-6}$ and $\lambda \sim 10^{-10}$ m) the typical refraction angles given by Eq. (2.8) range from few to few tens of microradians, hence, a posteriori, both projection and paraxial approximations hold.

2.2 The Simplest Phase-Sensitive Technique: Propagation-Based Imaging

The description of the interaction between an X-ray wave and a refractive object given so far is rather general and can serve as input to explain how many of the available phase-sensitive techniques work. As mentioned, to image the phase means to convert phase shift into intensity modulation. Broadly speaking, the plethora of techniques enabling phase imaging can be divided in into two groups, namely interferometric [15–18] and non-interferometric [19–22]. A complete description of the contrast formation mechanisms in all the phase-sensitive techniques goes beyond the scope of this work and the reader is referred to comprehensive reviews [23, 24] or books [8, 13].

In this section we focus on propagation-based (PB) imaging (note that in the literature other synonyms as in-line holography or free-space-propagation imaging can be found), which is arguably the simplest non-interferometric phase-sensitive technique to implement. Stripped down to its essence, PB imaging consists in distancing the detector from the refractive object, leaving the perturbed wavefront to propagate freely in space, as sketched in Fig. 2.2 [21]. To explain how the contrast is formed on the detector we revert our wave model to a simpler ray-tracing (or geometrical optics) approach, where X-rays are considered to be bullet-like entities whose path in each point is defined to be parallel to the local wave vector [25–27]. Moreover, it is assumed that the refractive object located in the xy plane is small compared with its distance z_1 from the image plane $x_1 y_1$. Let be $I(x, y)$ the X-ray beam intensity emerging from the object; in the previous section we saw that this quantity is proportional to the wave square modulus, thus containing only attenuation information. Nevertheless, phase-effects manifest themselves at some propagation distance, downstream of the object. In fact, as a function of its position (x, y) on the object plane, each 'ray' is be deviated by a small angle α specified by Eq. (2.8), thus impinging on the detector at the position (x_1, y_1) given by

$$\begin{cases} x_1 \simeq x + z_1 \alpha_x(x, y) \\ y_1 \simeq y + z_1 \alpha_y(x, y) \end{cases} \tag{2.9}$$

where α_x and α_y are the projections of α in the planes xz and yz, respectively

$$\alpha_x = \frac{1}{k} \frac{\partial}{\partial x} \Phi(x, y) \text{ and } \alpha_y = \frac{1}{k} \frac{\partial}{\partial y} \Phi(x, y) \tag{2.10}$$

Equation (2.9) expresses simply the coordinate transformation that maps each ray from the object to the detector plane [28]. Therefore, by calculating the transformation Jacobian, one can write the intensity detected in the image plane as

$$\begin{aligned} I(x_1, y_1) &= I(x, y) \left| \frac{\partial(x_1, y_1)}{\partial(x, y)} \right|^{-1} \\ &= I(x, y) \left| \begin{matrix} 1 + z_1 \frac{\partial \alpha_x}{\partial x} & z_1 \frac{\partial \alpha_x}{\partial y} \\ z_1 \frac{\partial \alpha_y}{\partial x} & 1 + z_1 \frac{\partial \alpha_y}{\partial y} \end{matrix} \right|^{-1} \\ &\simeq I(x, y) \left(1 + \frac{z_1}{k} \nabla^2 \Phi(x, y) \right)^{-1} \end{aligned} \tag{2.11}$$

where ∇^2 is the Laplacian in the object plane and the approximation is obtained by neglecting the terms $o(z_1^2 \lambda^2)$. This assumption seems rather reasonable since, in a typical PB setup, z_1 is of the order of meters while $\lambda \sim 10^{-10}$ m. In those cases in which $z_1 k \nabla^2 \Phi(x, y) \ll 1$, i.e. when the phase contrast is 'weak' [29], a first-order Taylor expansion can be applied to Eq. (2.11), yielding

$$I(x_1, y_1) \simeq I(x, y) \left(1 - \frac{z_1}{k} \nabla^2 \Phi(x, y) \right)$$
$$= I_0 e^{-2k \int \beta(x,y,z)\, dz} \left(1 - \frac{z_1}{k} \nabla^2 \Phi(x, y) \right) \tag{2.12}$$

where I_0 is the X-ray intensity impinging on the object. This equation is the main result of this chapter since it explains the contrast formation principle of PB imaging. In the limit of null propagation distance $z_1 = 0$, the previous equation reduces to the Beer-Lambert law, hence only the attenuation properties of the material contribute to image formation. Conversely, by increasing z_1 another source of contrast, the phase contrast, which is proportional to the Laplacian of the phase shift, comes into play. In the case of a planar impinging wavefront, phase contrast increases linearly with the propagation distance and it is more evident at the boundaries or at sharp interfaces of the refractive object, where the phase shift changes abruptly, producing the so-called edge enhancement effect [30], as shown in Fig. 2.3. It is worth noting that, even if the ray-optical approach may be seen as a naive approximation, the same expression for intensity found in Eq. (2.12) can be demonstrated following a rigorous wave model, taking as a starting point either the (near-field) Fresnel diffraction integral or the transport-of-intensity equation [12, 13].
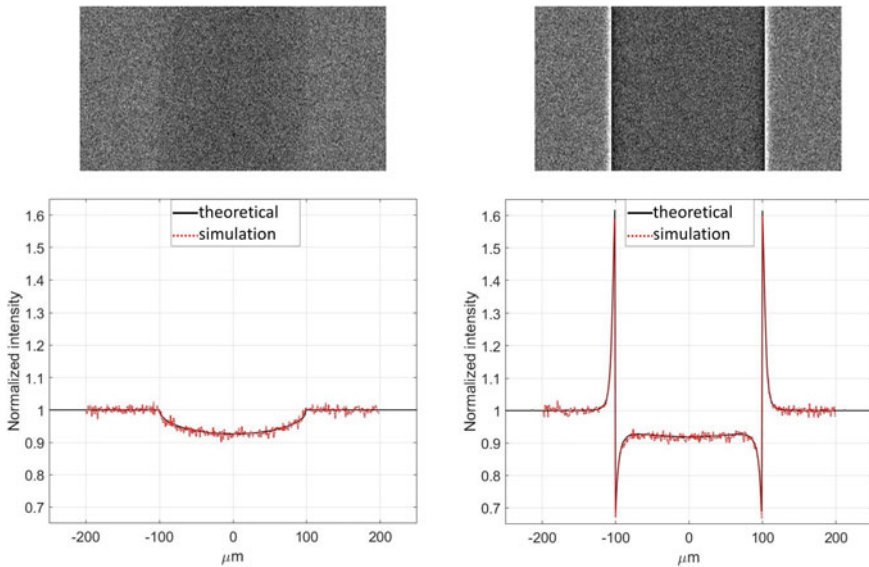
Fig. 2.3 Simulation of a 200 μm thick PMMA wire imaged at 10 keV with null propagation distance (top-left) and with 1 m of propagation distance (top-right). On the bottom the two corresponding intensity profiles matching the theoretical predictions

2.3 Effects of Finite Source Size, Detector Resolution and Near-Field Limit

So far, the whole derivation has been carried on under the hypothesis of a perfectly coherent plane wave (i.e. monochromatic and produced by a point-like source at infinite distance) and an ideal detector with a arbitrarily high spatial resolution. As it always happens, real life is sub-ideal and any deviation from both the previous assumptions can deeply affect the detected image. To study these effects let us consider a source located at a finite distance z_0 from the object plane and with a finite dimension characterized by a spatial intensity distribution $\mathrm{PSF_{src}}$. At the same time let the detector be pixelated, having a finite spatial resolution and point spread function $\mathrm{PSF_{det}}$ which is usually of the order of one or few pixels. Let also introduce a geometrical magnification factor $M = (z_0 + z_1)/z_0$ accounting for the relative positions of source, object and detector. In this case, the detected intensity I' reads

$$
\begin{aligned}
I'(x_1, y_1; M) &= I(x_1, y_1; M) * \left(\mathrm{PSF_{src}} \left(\frac{x_1}{M-1}, \frac{y_1}{M-1} \right) * \mathrm{PSF_{det}}(x_1, y_1) \right) \\
&= I(x_1, y_1; M) * \mathrm{PSF_{sys}}(x_1, y_1; M)
\end{aligned}
\tag{2.13}
$$

where $*$ denotes the convolution operator, $\mathrm{PSF_{sys}}$ is the convolution of the detector response function with the source referred to the detector plane, and $I(x_1, y_1; M)$ is the equivalent to the intensity of Eq. (2.12) when the magnification factor is accounted for [27]:

$$
I(x_1, y_1; M) = \frac{I(x, y)}{M^2} \left[1 - \frac{z_1}{kM} \nabla^2 \Phi(x, y) \right]
\tag{2.14}
$$

Equation (2.13) implies that the image detected in a real experiment is a blurred version of the image that would be obtained under ideal conditions and the amount of blurring depends on source distribution, detector response and geometry of the system. Given that phase-contrast manifests itself across sharp interfaces, thus contributing to the high frequency component of the image, the blurring introduced by $\mathrm{PSF_{sys}}$ affects primarily the phase content of the image, potentially smearing out completely the edge-enhancement effect as reported in Fig. 2.4. Taking a closer look to $\mathrm{PSF_{sys}}$ it can be demonstrated, by using rules of geometrical optics, that its width w goes as [31, 32]:

$$
w \sim \sqrt{s^2(M-1)^2 + d^2}
\tag{2.15}
$$

where s describes the source size and d the width of the detector PSF. This simple formula leads to some important considerations on the experimental implementation of PB imaging. In the majority of synchrotron-based PB experiments, the source can be considered to be ideal, meaning that its size is small and/or its distance from the object is much larger than the propagation distance (M is small): in these cases the first term in the addition of Eq. (2.15) can be neglected and the phase-contrast signal is
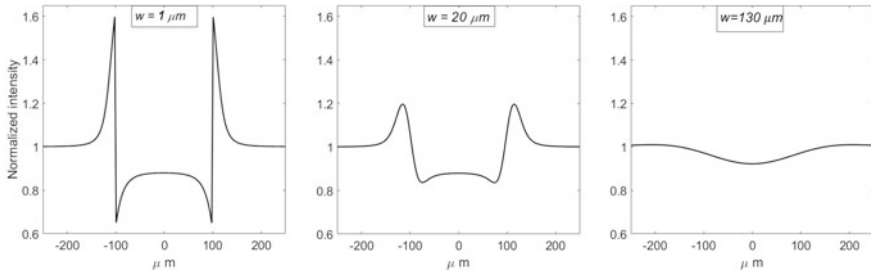
Fig. 2.4 Theoretical intensity profiles of a 200 μm thick PMMA wire convolved, from left to right, with Gaussian PSF_{sys} of full width half maximum w of 1, 20 and 130 μm respectively. To wider PSF_{sys} corresponds a loss of phase contrast due to the smearing of edge-enhancement effect

maximized by improving the detector spatial resolution and enlarging the propagation distance. On the contrary, for many conventional X-ray sources (e.g., rotating anode tubes), the source size is rather big and/or the magnification is high. In this case, any improvement in the detector resolution will not affect the visibility of phase effects since the magnitude of blurring w is dominated by the source contribution. For this reason, most of the conventional sources in use for medical applications are of no use in the field of PB phase-contrast imaging. Other practical considerations, along with the description of a dedicated PB imaging laboratory setup using a rotating anode source, can be found in Chap. 7, while more on the effects of pixel size and propagation distance is reported in Chap. 5.

Before concluding this section, some remarks on the applicability range of Eq. (2.12) should be pointed out. As stated previously, an analogous equation can be derived using the Fresnel diffraction integral in the near-field regime. This means that the given description of PB imaging technique holds for large Fresnel numbers, i.e. $N_F = a^2/(\lambda z_1) \gg 1$, where a is the smallest object's feature size of interest, which is usually related to the detector pixel size [8, 23]. This validity condition imposes an upper limit to the propagation distance (z_1) and a lower limit to the pixel size ($\sim a$), and implies that phase-contrast signal cannot be made arbitrarily large neither by increasing the propagation distance nor by decreasing the pixel size. For this reason, when setting up a PB imaging experiment, the N_F should be checked before using the aforementioned theoretical background for describing or analyzing experimental data. As an example, in the case of the experimental setup described throughout this work, a can be identified with the detector pixel size (60 μm), the propagation distance is in the order of few meters while the wavelength is a fraction of angstrom, resulting in Fresnel numbers larger than 10, so the near-field description holds. It should be noted that, conceptually, any PB imaging experimental setup can be used also in the opposite regime, i.e. far-field or Fraunhofer diffraction, provided that $N_F \ll 1$. A complete description of all the different working regimes of PB imaging can be obtained by means of the Fresnel-Kirchhoff diffraction integrals [11, 33] as illustrated in several works [16, 34, 35].

2.4   Inverting the Propagation: Phase-Retrieval

So far the image formation process in PB configuration has been described and, as a pivotal result, Eq. (2.12) was derived, expressing how the detected intensity depends on attenuation and phase properties of the illuminated object. However, many practical applications require to obtain separately both attenuation and phase-shift information rather than a phase-contrast image where their contributions are mixed [13]. The combination of this requirement with the experimentally desirable property of performing single-shot imaging results in an ill-posed problem: trying to retrieve simultaneously both phase (shift) and attenuation from Eq. (2.12) means to find solutions for two unknowns given only one equation. In the last two decades many workarounds to solve this problem, commonly known as phase-retrieval (PhR), have been derived, all of which have required multiple approximations to be made. Generally speaking, these approximations aim at reducing the number of unknowns in Eq. (2.12), thus making the expression invertible. As a first line discrimination, PhR algorithms can be split in two categories: some of them assume the sample to be non-absorbing or a 'pure phase' object, which is a suitable approximation for thin or low density samples; others require the sample to be composed of a single monomorphous material (often described as homogeneous). These and other approximations have been studied in detail in [36], listing similarities and differences between seven commonly used algorithms. In the following, a PhR algorithm falling in the second category is described and used throughout this work.

The algorithm was first proposed by Paganin and collaborators in 2002 and it is allegedly the most widely used in the PB imaging community [37]. Since this PhR technique stems from a particular version of the transport-of-intensity equation (TIE) describing a homogeneous object (TIE-Hom), it is worth starting by introducing the TIE itself [38]:

$$\nabla_{xy}\left[I(x, y; z = 0)\nabla_{xy}\Phi(x, y; z = 0)\right] = -k\frac{\partial I(x, y; z = 0)}{\partial z} \qquad (2.16)$$

where, for each function of space, the z coordinate is specified to unambiguously discriminate between the object plane ($z = 0$) and the image plane ($z = z_1$). This equation provides a relation between the (measurable) intensity and the object-induced phase shift under paraxial and projection approximations. Given this definition it is not surprising that TIE is equivalent to Eq. (2.12), as demonstrated in Appendix A. The following step is to introduce the monomorphicity condition, stating that the object is composed by a single material and both δ and β (or at least their ratio) are known. In this case, phase and intensity on the object plane can be written as

$$I(x, y; z = 0) = I_0 e^{-2k\beta t(x,y)} \text{ and } \Phi(x, y; z = 0) = -k\delta t(x, y) \qquad (2.17)$$

where $t(x, y)$ is the integrated object thickness along z direction and I_0 is the X-ray intensity impinging in the object plane. The homogeneity condition allows to express both the intensity and phase terms as a function of the same variable $t(x, y)$, thus reducing the number of unknowns from two to one. Substituting the definitions of Eq. (2.17) into Eq. (2.16), and making use of the following identity

$$- k\delta \nabla_{xy} \left[e^{-2k\beta t(x,y)} \nabla_{xy} t(x, y) \right] = \frac{\delta}{2\beta} \nabla_{xy}^2 e^{-2k\beta t(x,y)} \tag{2.18}$$

TIE reduces to its homogeneous version

$$\frac{\delta}{2\beta} \nabla_{xy}^2 \left[I_0 e^{-2k\beta t(x,y)} \right] = -k \frac{\partial I(x, y; z = 0)}{\partial z} \tag{2.19}$$

The last step of the derivation consists in finding the (approximate) expression of the derivative appearing in the right-hand side of the latter equation. Usually, it is approximated by the intensity difference between contact and image planes [12]

$$\frac{\partial I(x, y; z = 0)}{\partial z} \simeq \frac{I(x, y; z = z_1) - I(x, y; z = 0)}{z_1} \tag{2.20}$$

By inserting this approximation in Eq. (2.19) and re-arranging the terms we get

$$I(x, y; z = z_1) = \left(1 - \frac{z_1 \delta}{2k\beta} \nabla_{xy}^2 \right) I_0 e^{-2k\beta t(x,y)} \tag{2.21}$$

At this point the only unknown term is $t(x, y)$, hence TIE-Hom equation and can be solved. The solution provided by Paganin [37] makes use of the Fourier derivative theorem, yielding the projected thickness as

$$t(x, y) = -\frac{1}{2k\beta} \ln \left(\mathscr{F}^{-1} \left\{ \frac{\mathscr{F} [I(x, y; z = z_1)/I_0]}{1 + \frac{z_1 \delta}{2k\beta} |\mathbf{v}|^2} \right\} \right) \tag{2.22}$$

where $\mathscr{F}$ and $\mathscr{F}^{-1}$ denote the bi-dimensional Fourier transform and anti-transform, respectively, and $\mathbf{v} = (v_1, v_2)$ represents the Cartesian coordinates in the Fourier space. Once the projected thickness has been calculated it can be inserted in Eq. (2.17) to obtain both attenuation $I(x, y; z = 0)$ and phase $\Phi(x, y; z = 0)$ images.

The last two equations, i.e. (2.21) and (2.22), are the central result of this section; the former describes how the X-ray intensity propagate from the object to the image plane (forward propagation), the latter allows to revert this process by backpropagating (i.e. retrieving) the captured image to the object plane, as sketched in Fig. 2.5. To fully understand the effects of forward and backward propagation, it is convenient to adopt a signal processing approach where both processes are described as operators acting, respectively, on the object plane and the image plane intensity distributions [29]. From Eq. (2.21) the forward propagation operator is defined as
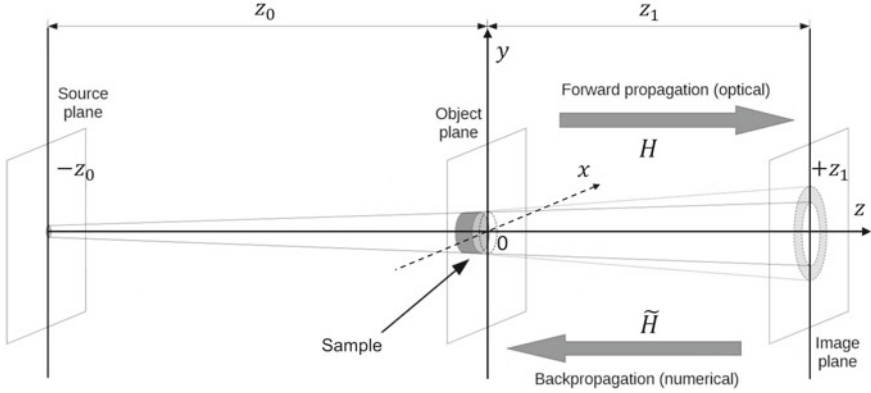
Fig. 2.5 Schematic representation of the (optical) propagation and following (numerical) phase-retrieval in a PB setup. The source plane is positioned in coordinate $-z_0$ along the z axis, the object plane defines the origin of the reference system while the image plane is positioned at z_1. H and $\tilde{H}$ denote the forward and backpropagation operators, respectively

$$H = \left(1 - \frac{z_1\delta}{2k\beta}\nabla^2_{xy}\right) \qquad (2.23)$$

which is an optical (i.e. pre-detection) deconvolution. Due the presence of the Laplace operator, H affects the image by boosting its high spatial frequency component, hence the image spatial resolution. It is worth noting that this effect, associated with PB imaging, has already been described in the previous section under the name of edge-enhancement. Conversely, the core of PhR algorithm is a bell-shaped filter in Fourier domain that, from Eq. (2.22), can be written as

$$\tilde{H} = \left(1 + \frac{z_1\delta}{2k\beta}|\mathbf{v}|^2\right)^{-1} \qquad (2.24)$$

The effect of this filter, similar in a sense to that of a (numerical) convolution with any low-pass filter, is to reduce the image noise at cost of a worse spatial resolution [39, 40]. Anyway, the remarkable property of $\tilde{H}$ is that the resolution loss exactly compensate the spatial resolution boost due to H, i.e. to the forward propagation. Despite its apparent circularity, the combination of the forward (optical) propagation and the subsequent backward (numerical) inversion results in an image which is equivalent, up to a logarithmic transformation, to the image that would have been obtained in the object plane (i.e. the attenuation image), but with a dramatic noise reduction [41–43]. As explained by Gureyev and colleagues [29], the origin of such 'unreasonable' image quality enhancement lies in the fact that the propagation operator is an optical deconvolution (as opposed to a numerical one) which is applied prior to the image detection, thus before the generation of detection noise which is not propagated by the deconvolution itself. In terms of image quality this noteworthy effect is of paramount

importance since, in general, detail visibility in any radiographic technique strongly depends on the image noise content. An experimental proof of this effect, applied to tomographic images of breast specimens, will be provided in Chap. 5.

2.5 Single- and Two-Materials Approaches to Phase Retrieval

In the derivation of the PhR filter allowing to invert TIE-Hom equation it is assumed that the investigated object is homogeneous with a known δ/β, meaning that the phase-shift and attenuation properties of the sample are proportional throughout the sample. In order to take into account the presence of two (homogeneous) materials of interest within the sample (e.g., glandular details embedded in an adipose background in breast imaging), the PhR filter reported in Eq. (2.24), referred to as single-material, can be slightly modified to

$$\tilde{H}_{2\text{mat}} = \left(1 + \frac{z_1}{2k} \frac{\delta_1 - \delta_2}{\beta_1 - \beta_2} |\mathbf{v}|^2 \right)^{-1} \tag{2.25}$$

where the δ/β term has been replaced by $(\delta_1 - \delta_2)/(\beta_1 - \beta_2)$, and the subscripts refer to the two materials of interest [36]. In qualitative terms, the application of PhR allows in general to compensate for the edge-enhancement effect arising at the object interfaces upon the propagation process. Specifically, the single-material PhR allows to exactly compensate for the edge enhancement at vacuum/sample or, in practice, air/sample interfaces. Conversely, the two-materials PhR exactly compensates the edge enhancement across interfaces of two given materials embedded within the sample. In this perspective, the phase retrieval can be seen as a virtual lens which, by tuning the parameter δ/β, enables to focus upon a particular interface of interest [44]. In the case of interest of breast imaging at energies around 30 keV, δ/β is of the order of 2×10^3 for breast tissue in the single-material PhR, while $(\delta_1 - \delta_2)/(\beta_1 - \beta_2)$ is of the order of 1×10^3 for glandular/adipose interfaces in the two-materials PhR. This means that, from a signal processing perspective, the application of single-material PhR would result in a smoother image (i.e. lower noise and higher blur) with respect to the two-materials PhR [45]. Since both approaches will be used throughout this work, the type of PhR filter used will be specified for each reconstructed dataset.

2.6 Tomographic Reconstruction

While for thin bi-dimensional samples a planar image can provide sufficient information on the scanned object, for three-dimensional bulk samples (e.g., human breast), planar techniques may fail in providing an accurate description due to superposition

effects. In this context, X-ray tomography is capable of overcoming such limitation, providing a fully three-dimensional map of a given object property.

A tomographic acquisition requires several planar 'views' of the sample, or projections, obtained by exposing the object to the X-ray beam at different angles. Each projection, collected at an angle θ, will be the line integral through the sample of a given object spatial distribution function $o(x, y, z)$:

$$p_\theta(x, y) = \int o(x \cos \theta - z \sin \theta, y, x \sin \theta + z \cos \theta) \, dz \qquad (2.26)$$

where the integral extends along the object thickness, y identifies the rotation axis and xz defines the tomographic plane through the object (see Fig. 2.2). Equation (2.26) identifies the Radon transform of the function $o(x, y, z)$ [46]. To reconstruct a tomographic image means to recover the spatial distribution $o(x, y, z)$ given a sufficient number of projection images $p_\theta(x, y)$ or, equivalently, to invert the Radon transform. Considering a parallel X-ray geometry, this can be accomplished by acquiring the projection images over 180 degrees and by applying the well-known filtered-back-projection (FBP) algorithm [47]:

$$o(x, y, z) = \int_0^\pi \left[\int_{-\infty}^{+\infty} P_\theta(q; y) |q| G(q) e^{2\pi i q x} \, dq \right] d\theta \qquad (2.27)$$

where $P_\theta(q; y)$ is the 1D Fourier transform of the projection p_θ along the direction x, $|q|$ is the ramp filter in the frequency domain, and $G(q)$ is the apodization filter used to limit the high spatial frequency contribution in the reconstruction. Of note, in parallel geometry, FBP does not involve the variable y, hence each reconstructed 'slice', identified by a given position y, is independent from the others.

Considering that conventional attenuation-based imaging can be seen as a special case of PB imaging at null propagation distance, rearranging Eq. (2.12) we can write

$$p_0^{\text{abs}}(x, y) = -\ln \frac{I(x, y)}{I_0} = 2k \int \beta(x, y, z) \, dz = \int \mu(x, y, z) \, dz \qquad (2.28)$$

where, for the sake of notation simplicity, the considered projection angle is $\theta = 0$. Given Eq. (2.28), the linear attenuation coefficient map $\mu(x, y, z)$ can be immediately identified with the object distribution $o(x, y, z)$ to be reconstructed by means of the FBP algorithm. The same formalism can be extended to the more general case of a finite propagation distance z_1, provided that Eq. (2.12) is conveniently re-written as

$$I(x_1, y_1) = I_0 e^{-\int \mu(x,y,z) \, dz} \left(1 - \frac{z_1}{k} \nabla_{xy}^2 \Phi(x, y) \right) \simeq I_0 e^{-\left[\int \mu(x,y,z) \, dz + \frac{z_1}{k} \nabla_{xy}^2 \Phi(x,y) \right]} \qquad (2.29)$$

where, in the weak phase-contrast assumption, the term in parenthesis is identified with the Taylor expansion of an exponential term [48]. Starting from the previous

expression, and recalling that $\Phi(x, y) = -k \int \delta(x, y, z)\, dz$, the projection image acquired in PB configuration reads

$$p_0^{\text{PB}}(x, y) = -\ln \frac{I(x_1, y_1)}{I_0} = \int \mu(x, y, z)\, dz - z_1 \nabla_{xy}^2 \int \delta(x, y, z)\, dz \quad (2.30)$$

In this case, the tomographic reconstruction of the first term provides the attenuation coefficient map whereas the second term corresponds to the three-dimensional Laplacian of the decrement from unity of the refractive index $\delta(x, y, z)$. In summary, for PB imaging, the reconstructed distribution is approximated by

$$o^{\text{PB}}(x, y, z) = \mu(x, y, z) - z_1 \nabla_{xyz}^2 \delta(x, y, z) \quad (2.31)$$

Equation (2.31) is of great importance since it proves that, similarly to the planar case, a tomographic map reconstructed from PB projections will be similar to the (conventional) attenuation map except for object interfaces or sharp edges, where the (three-dimensional) Laplacian of δ is expected to be significantly different from zero.

Finally, the tomographic reconstruction of phase-retrieved projections should be considered. Following the Paganin's approach, in the derivation of the PhR formula the imaged object is assumed to be homogeneous, so its attenuation and phase-shift properties (or at least their ratio) are constant throughout the volume. The application of the phase retrieval yields, for each projection, the object projected thickness, which, given the homogeneity assumption, is proportional to the line integrals of both $\mu(x, y, z)$ and $\delta(x, y, z)$.

$$p_0^{\text{PhR}}(x, y) = t(x, y) = \frac{1}{\mu_{\text{in}}} \int \mu(x, y, z)\, dz = \frac{1}{\delta_{\text{in}}} \int \delta(x, y, z)\, dz \quad (2.32)$$

where the proportionality constants $1/\mu_{\text{in}}$ and $1/\delta_{\text{in}}$ are input parameters of the PhR filter as reported in Eq. (2.22). Given this definition of the projection image, the tomographic reconstructed quantity will be

$$o^{\text{PhR}}(x, y, z) = \frac{1}{\mu_{\text{in}}} \mu(x, y, z) = \frac{1}{\delta_{\text{in}}} \delta(x, y, z) \quad (2.33)$$

Of note, starting from phase-retrieved projections, the reconstructed image is found to be proportional to the (conventional) attenuation image $\mu(x, y, z)$, meaning that the image contrast is equal to the attenuation contrast. In case of medical applications, this is of great importance since tomographic images reconstructed after applying the PhR procedure can be calibrated in terms of linear attenuation coefficients, which is the standard procedure in conventional X-ray tomography [49]. More details on the phase-retrieval effects on the reconstructed image will be discussed in Chap. 5.

References

1. Brailsford JF (1946) Roentgen's discovery of x rays: their application to medicine and surgery. Br J Radiol 19(227):453–461. https://doi.org/10.1259/0007-1285-19-227-453
2. Mould RF (1980) A History of X-rays and radium. IPC Building & ContraCT Journals Limited
3. Compton AH (1927) Nobel prize-winner tells of discoveries: X-rays as a branch of optics. Sci News-Lett 12(349):387–388. https://doi.org/10.2307/3902440
4. Hounsfield GN (1980) Computed medical imaging. J Comput Assis Tomogr 4(5):665. https://doi.org/10.1097/00004728-198010000-00017 (Nobel lecture, 8 Dec 1979)
5. Taylor JA (2018) TS imaging. http://ts-imaging.science.unimelb.edu.au/Services/Simple/
6. Als-Nielsen J, McMorrow D (2011) Elements of modern X-ray physics. Wiley, New York. https://doi.org/10.1002/9781119998365
7. Griffiths DJ (2017) Introduction to electrodynamics.
8. Rigon L (2014) X-ray imaging with coherent sources. In: Brahme A (ed) Comprehensive biomedical physics, vol 2. Elsevier, pp 193–216. https://doi.org/10.1016/B978-0-444-53632-7.00209-4
9. Lewis R (2004) Medical phase contrast X-ray imaging: current status and future prospects. Phys Med Biol 49(16):3573. https://doi.org/10.1088/0031-9155/49/16/005
10. Zhou S-A, Brahme A (2008) Development of phase-contrast X-ray imaging techniques and potential medical applications. Phys Med 24(3):129–148. https://doi.org/10.1016/j.ejmp.2008.05.006
11. Born M, Wolf E (1999) Principles of optics, 7th (expanded) edition. Cambridge University Press, Cambridge, UK, p 890. https://doi.org/10.1017/CBO9781139644181
12. Paganin D (2006) Coherent X-ray optics. Number 6 in Oxford series on synchrotron radiation. Oxford University Press on Demand. https://doi.org/10.1093/acprof:oso/9780198567288.001.0001
13. Pelliccia D, Kitchen MJ, Morgan KS (2018) Theory of X-ray phase-contrast imaging. In: Russo P (ed) Handbook of X-ray imaging: physics and technology. Taylor and Francis, pp 971–997. ISBN 978-1-4987-4152-1. https://doi.org/10.1201/9781351228251 (chapter 49)
14. Cunningham JR, Johns HE (1983) The physics of radiology. Springfield: Charles C. Thosmas. https://doi.org/10.1118/1.595545
15. Bonse U, Hart M (1965) An X-ray interferometer. Appl Phys Lett 6(8):155–156. https://doi.org/10.1063/1.1754212
16. Snigirev A, Snigireva I, Kohn V, Kuznetsov S, Schelokov I (1995) On the possibilities of X-ray phase contrast microimaging by coherent high-energy synchrotron radiation. Rev Sci Instrum 66(12):5486–5492. https://doi.org/10.1063/1.1146073
17. Momose A (1995) Demonstration of phase-contrast X-ray computed tomography using an X-ray interferometer. Nucl Instrum Methods Phys Res Sect A: Accelerators, Spectrometers, Detectors Assoc Equipment 352(3):622–628. https://doi.org/10.1016/0168-9002(95)90017-9
18. Cloetens P, Guigay J, De Martino C, Baruchel J, Schlenker M (1997a) Fractional talbot imaging of phase gratings with hard x rays. Opt Lett 22(14):1059–1061. https://doi.org/10.1364/OL.22.001059
19. Davis T, Gao D, Gureyev T, Stevenson A, Wilkins S (1995) Phase-contrast imaging of weakly absorbing materials using hard x-rays. Nature 373(6515):595. https://doi.org/10.1038/373595a0
20. Ingal V, Beliaevskaya E (1995) X-ray plane-wave topography observation of the phase contrast from a non-crystalline object. J Phys D Appl Phys 28(11):2314. https://doi.org/10.1088/0022-3727/28/11/012
21. Wilkins S, Gureyev TE, Gao D, Pogany A, Stevenson A (1996) Phase-contrast imaging using polychromatic hard x-rays. Nature 384(6607):335. https://doi.org/10.1038/384335a0
22. Olivo A, Arfelli F, Cantatore G, Longo R, Menk R, Pani S, Prest M, Rigon L, Tromba G, Vallazza E et al (2001) An innovative digital imaging set-up allowing a low-dose approach to phase contrast applications in the medical field. Med Phys 28(8):1610–1619. https://doi.org/10.1118/1.1388219

23. Bravin A, Coan P, Suortti P (2012) X-ray phase-contrast imaging: from pre-clinical applications towards clinics. Phys Med Biol 58(1):R1. https://doi.org/10.1088/0031-9155/58/1/R1

24. Olivo A, Castelli E (2014) X-ray phase contrast imaging: from synchrotrons to conventional sources. Rivista del nuovo cimento 37(9):467–508. https://doi.org/10.1393/ncr/i2014-10104-8

25. Ishisaka A, Ohara H, Honda C (2000) A new method of analyzing edge effect in phase contrast imaging with incoherent x-rays. Opt Rev 7(6):566–572. https://doi.org/10.1007/s10043-000-0566-z

26. Monnin P, Bulling S, Hoszowska J, Valley J-F, Meuli R, Verdun F (2004) Quantitative characterization of edge enhancement in phase contrast X-ray imaging. Med Phys 31(6):1372–1383. https://doi.org/10.1118/1.1755568

27. Peterzol A, Olivo A, Rigon L, Pani S, Dreossi D (2005) The effects of the imaging system on the validity limits of the ray-optical approach to phase contrast imaging. Med Phys 32(12):3617–3627. https://doi.org/10.1118/1.2126207

28. Gureyev T, Wilkins S (1998) On X-ray phase imaging with a point source. JOSA A 15(3):579–585. https://doi.org/10.1364/JOSAA.15.000579

29. Gureyev TE, Nesterets YI, Kozlov A, Paganin DM, Quiney HM (2017) On the "unreasonable" effectiveness of transport of intensity imaging and optical deconvolution. JOSA A 34(12):2251–2260. https://doi.org/10.1364/JOSAA.34.002251

30. Spanne P, Raven C, Snigireva I, Snigirev A (1999) In-line holography and phase-contrast microtomography with high energy x-rays. Phys Med Biol 44(3):741. https://doi.org/10.1088/0031-9155/44/3/016

31. Gureyev TE, Nesterets YI, Stevenson AW, Miller PR, Pogany A, Wilkins SW (2008) Some simple rules for contrast, signal-to-noise and resolution in in-line X-ray phase-contrast imaging. Opt Express 16(5):3223–3241. https://doi.org/10.1364/OE.16.003223

32. Brombal L, Kallon G, Jiang J, Savvidis S, De Coppi P, Urbani L, Forty E, Chambers R, Longo R, Olivo A et al (2019b) Monochromatic propagation-based phase-contrast microscale computed-tomography system with a rotating-anode source. Phys Rev Appl 11(3):034004. https://doi.org/10.1103/PhysRevApplied.11.034004

33. Cowley JM (1995) Diffraction physics. Elsevier. https://doi.org/10.1016/B978-0-444-82218-5.X5000-7

34. Pogany A, Gao D, Wilkins S (1997) Contrast and resolution in imaging with a microfocus X-ray source. Rev Sci Instrum 68(7):2774–2782. https://doi.org/10.1063/1.1148194

35. Arfelli F, Assante M, Bonvicini V, Bravin A, Cantatore G, Castelli E, Dalla Palma L, Di Michiel, M, Longo R, Olivo A et al (1998) Low-dose phase contrast X-ray medical imaging. Phys Med Biol 43(10):2845. https://doi.org/10.1088/0031-9155/43/10/013

36. Burvall A, Lundström U, Takman PA, Larsson DH, Hertz HM (2011) Phase retrieval in X-ray phase-contrast imaging suitable for tomography. Opt Express 19(11):10359–10376. https://doi.org/10.1364/OE.19.010359

37. Paganin D, Mayo S, Gureyev TE, Miller PR, Wilkins SW (2002) Simultaneous phase and amplitude extraction from a single defocused image of a homogeneous object. J Microsc 206(1):33–40. https://doi.org/10.1046/j.1365-2818.2002.01010.x

38. Teague MR (1983) Deterministic phase retrieval: a green's function solution. JOSA 73(11):1434–1441. https://doi.org/10.1364/JOSA.73.001434

39. Barrett HH, Myers KJ (2003) Foundations of image science. Wiley, New York. https://doi.org/10.1117/1.1905634

40. Gureyev T, Nesterets Y, de Hoog F (2016) Spatial resolution, signal-to-noise and information capacity of linear imaging systems. Opt Express 24(15):17168–17182. https://doi.org/10.1364/OE.24.017168

41. Nesterets YI, Gureyev TE (2014) Noise propagation in X-ray phase-contrast imaging and computed tomography. J Phys D Appl Phys 47(10):105402. https://doi.org/10.1088/0022-3727/47/10/105402

42. Kitchen MJ, Buckley GA, Gureyev TE, Wallace MJ, Andres-Thio N, Uesugi K, Yagi N, Hooper SB (2017) CT dose reduction factors in the thousands using X-ray phase contrast. Sci Rep 7(1):15953. https://doi.org/10.1038/s41598-017-16264-x

43. Brombal L, Donato S, Dreossi D, Arfelli F, Bonazza D, Contillo A, Delogu P, Di Trapani, V, Golosio B, Mettivier G et al (2018b) Phase-contrast breast CT: the effect of propagation distance. Phys Med Biol 63(24):24NT03. https://doi.org/10.1088/1361-6560/aaf2e1

44. Beltran M, Paganin D, Uesugi K, Kitchen M (2010) 2D and 3D X-ray phase retrieval of multi-material objects using a single defocus distance. Opt Express 18(7):6423–6436. https://doi.org/10.1364/OE.18.006423

45. Brombal L, Golosio B, Arfelli F, Bonazza D, Contillo A, Delogu P, Donato S, Mettivier G, Oliva P, Rigon L et al (2018c) Monochromatic breast computed tomography with synchrotron radiation: phase-contrast and phase-retrieved image comparison and full-volume reconstruction. J Med Imaging 6(3):031402. https://doi.org/10.1117/1.JMI.6.3.031402

46. Deans SR (2007) The Radon transform and some of its applications. Courier Corporation. https://doi.org/10.1016/S0079-6638(08)70123-9

47. Buzug TM (2011) Computed tomography. In: Springer handbook of medical technology. Springer, Berlin, pp 311–342. https://doi.org/10.1007/978-3-540-39408-2

48. Cloetens P, Pateyron-Salomé M, Buffiere J, Peix G, Baruchel J, Peyrin F, Schlenker M (1997b) Observation of microstructure and damage in materials by phase sensitive radiography and tomography. J Appl Phys 81(9):5878–5886. https://doi.org/10.1063/1.364374

49. Piai A, Contillo A, Arfelli F, Bonazza D, Brombal L, Cova MA, Delogu P, Trapani VD, Donato S, Golosio B, Mettivier G, Oliva P, Rigon L, Taibi A, Tonutti M, Tromba G, Zanconati F, Longo R (2019) Quantitative characterization of breast tissues with dedicated CT imaging. Phys Med Biol 64(15):155011. https://doi.org/10.1088/1361-6560/ab2c29